Mesoscale Ocean Processes: The Critical Role of Stratification in the Icelandic Region

Charly de Marez [1], Clara R. Vives [2], Esther Portela Rodriguez[3], Angel Ruiz-Angulo [1]

[1]University of Iceland, Reykjavík, Iceland
[2]Globe Institute, Section for Geobiology, University of Copenhagen, Denmark
[3]Univ Brest, CNRS, IRD, Ifremer, Laboratoire d'Océanographie Physique et Spatiale, Plouzané, France

Key Points:

- High-resolution SWOT satellite data, *in situ* data, and numerical models are used to analyze ocean dynamics around Iceland
- North of Iceland, the shallow upper layer creates a "low-energy zone" with reduced energy at the mesoscale
- South of Iceland, the deep upper layer boosts the mesoscale eddy generation through baroclinic instability

Corresponding author: Charly de Marez, `charly@hi.is`

Abstract

The oceanic region around Iceland, a key component of the Atlantic Meridional Overturning Circulation, plays a critical role in global climate through its complex system of surface and subsurface currents. Using high-resolution SWOT satellite data, *in situ* observations, and idealized numerical simulations, this study reveals two distinct dynamical regimes in this region. South of Iceland, the mesoscale eddy field is energetic. In contrast, north of Iceland, the shallow upper layer inhibits baroclinic instability and eddy generation, resulting in a low-energy "eddy desert" — a phenomenon observed synoptically for the first time at SWOT's unprecedented resolution. This new understanding of Iceland's dynamical regimes highlights the role of stratification in mesoscale variability. Analyzing Biogeochemical-Argo float data, it also suggests an impact of mesoscale regimes on the local biogeochemical cycles, with implications for primary production and carbon cycling as stratification patterns shift with climate change.

Plain Language Summary

The waters around Iceland are an important part of the global climate system, influencing ocean currents and climate patterns. In this study, we used cutting-edge satellite data, ocean measurements, and computer models to investigate the behavior of ocean currents in the region. We discovered two distinct ocean zones around Iceland. South of Iceland, strong ocean currents create a turbulent flow. North of Iceland, however, the water is more stable, and the ocean is much calmer, with fewer currents and less mixing. This creates a "low-energy zone" where the usual ocean activity is limited. Our high-resolution data captured this unique, and previously unexplored feature. This study helps us understand how the movement of water around Iceland affects the ocean environment, with important implications for climate change and the future of marine ecosystems, as warmer temperatures may change these ocean patterns.

1 Introduction

The oceanic region surrounding Iceland plays a vital role in the Atlantic Meridional Overturning Circulation (AMOC), a major driver of global climate (Buckley & Marshall, 2016). Surface and subsurface currents in this area are shaped by both, regional ocean dynamics and complex topographic features, influencing the exchange of water masses between the Arctic and Atlantic oceans (Brakstad, Gebbie, et al., 2023). To the north of Iceland, the Iceland Sea is encompassed by the Greenland-Iceland Ridge and the Jan Mayen Ridge, acting as a physical barrier between the Arctic and Atlantic waters (Fig. 1). To the east, the Iceland-Faroe Ridge separates the Norwegian Sea and the Iceland Basin, while in the south of Iceland, the Reykjanes Ridge defines the boundary between the Iceland Basin and the Irminger Sea. The surface circulation is dominated by warm and saline North Atlantic waters flowing from the southwest. It is composed of the North Atlantic Current (NAC) which flows into the Iceland Basin, and the Irminger Current (IC) which flows into the Irminger Sea and detaches into the North Icelandic Irminger Current (NIIC) flowing clockwise reaching the north of Iceland (Hansen & Østerhus, 2000). The other main surface current is the East Greenland Current (EGC), transporting cold and fresh polar waters mainly southward along the east coast of Greenland. A small component of this branch is advected by the NIIC forming the East Icelandic Current (EIC, Logemann et al., 2013; Semper et al., 2022) . At mid-depths, northeast of Iceland, the North Icelandic Jet (NIJ) injects a small portion of dense water into the Denmark Strait (Jonsson & Valdimarsson, 2004; Casanova-Masjoan et al., 2020). All of these currents transport water masses that, together with the deep cold and denser waters: Iceland Scotland Overflow Water (ISOW) and the Denmark Strait Overflow Waters (DSOW), are key components of the AMOC.

Over the last two decades, our understanding of regional circulation in this area has steadily improved. However, the dynamics at smaller scales, particularly at the mesoscale and below, remain poorly understood. This is due to a scarcity of *in situ* data (Beaird et al., 2013) and the inability of numerical models and satellite data, until now, to resolve these scales both south and north of Iceland. In the Iceland Basin, several studies have documented the presence of mesoscale eddies, examining their origins, variability, and impact on regional circulation and nutrient distribution (Mahadevan et al., 2012; Godø et al., 2012; Zhao et al., 2018a; Soman et al., 2022; Z. Zhang et al., 2024; Johnson et al., 2024; Voet et al., 2024). These studies rely on AVISO-derived satellite altimetry ($1/4°$ resolution), which is at the limit of what is needed to resolve the mesoscale eddy field in the region (eddies in the Iceland Basin have an average radius of 50 km; see Soman et al., 2022). However, north of Iceland, in the Iceland Sea, pre-SWOT satellite altimetry has been largely ineffective due to the smaller deformation radius and the correspondingly small eddy sizes ($\mathcal{O}(10)$ km; Chelton et al., 1998). Past studies have primarily focused on regions bordering Norway or on large, semi-permanent structures such as the Lofoten Vortex (Bosse et al., 2019) and intense Norwegian Sea eddies, which are influenced by their Atlantic water component (Bashmachnikov et al., 2023). Thus, mesoscale-focused studies are scarce north of Iceland and *absent in the Iceland Sea*.

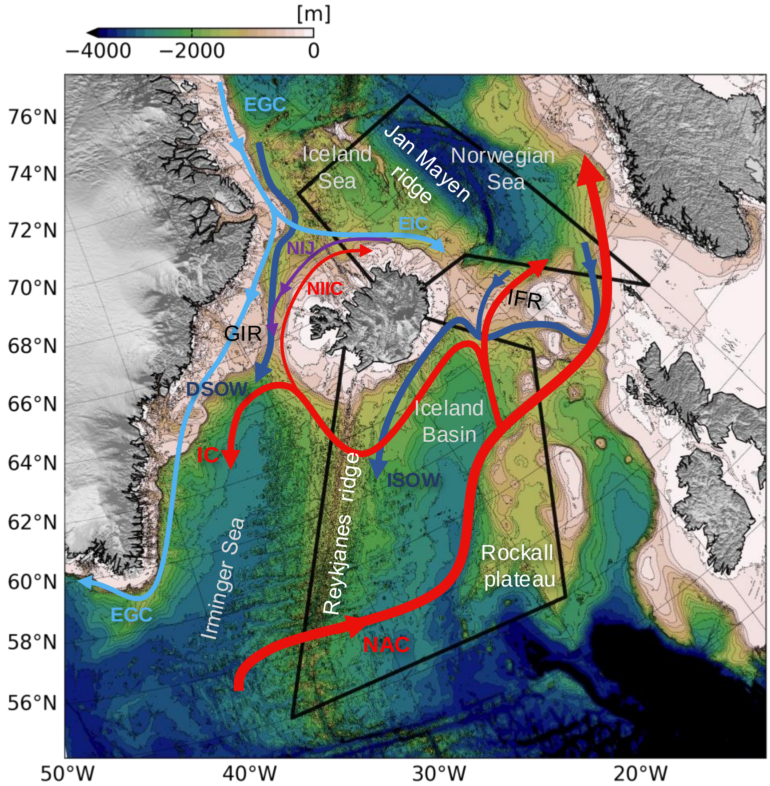

Figure 1. Bathymetry around Iceland highlighting the main topographic features, basins and seas; IFR and GIR stand for Iceland-Faroe Ridge and Greenland-Iceland Ridge, respectively. The areas we denominate as "south of Iceland" and "north of Iceland" in the study are indicated by the black solid lines. Bold arrows show schematic pathways of the main currents in the area: the North Atlantic Current (NAC), the East Greenland Current (EGC), the East Icelandic Current (EIC), the North Icelandic Jet (NIJ) and the North Icelandic Irminger Current (NIIC); dark blue arrows show the pathway of the two main bottom water masses flowing south: the Denmark Strait Overflow Waters (DSOW) and the Iceland Scotland Overflow Water (ISOW).

The surface currents around Iceland advect and mix the water masses. They shape the characteristic thermocline stratification and the mixed layer depth in the Iceland Basin, Iceland Sea and Norwegian Sea. The mixed layer is the uppermost layer of the Ocean, which is in direct contact with the atmosphere, where exchanges of heat, oxygen, carbon, and other tracers take place (Bindoff et al., 2019; Sallée et al., 2021). The physical processes within this layer influence injection of tracers into the ocean interior, including the oceanic CO_2 uptake and nutrient cycles, which are key components in the regulation of the Earth's climate (Ólafsson, 2003; Ruiz et al., 2019). At smaller scales, particular processes, such as meso and submesoscale eddies, modulate the mixed layer depth and enhance vertical fluxes through eddy-driven upwelling and downwelling (McGillicuddy et al., 2007; Mahadevan et al., 2012). Eddies therefore act as hotspots for primary production and carbon sink from the surface to the ocean interior (Ruiz et al., 2019). Stratification changes in the upper-ocean layers have been reported in the last 50 years as the result of changes in temperature and salinity (in particular saltier and warmer surface water, see Polyakov et al., 2017; Dai et al., 2019). These changes are particularly faster in the region around Iceland than the global average and are among the critical variables within the IPCC reports (Bindoff et al., 2019; Sallée et al., 2021).

As sea surface temperatures continue to increase (Bindoff et al., 2019; Pörtner et al., 2019), it is critical to understand how oceanic currents variability may change in a warming and potentially more stratified ocean, ultimately having implications for ocean productivity, carbon uptake and sequestration. In this study, we analyze the characteristics of mesoscale ocean dynamics around Iceland, using newly released SWOT satellite data, ship-based observations, numerical modeling, and Argo float data. We compare the regions north and south of Iceland; the northern region encompasses the Iceland Sea and the Norwegian Sea, while the southern region corresponds mainly with the Iceland basin, see definition in Fig. 1. We demonstrate the existence of two distinct dynamical regimes. On the one hand, the southern region consist of highly energetic *balanced geostrophic turbulence* (hereafter called *turbulence*, or *turbulent flow* for conciseness) with intense mesoscale activity. On the other hand, the northern region presents a stark contrast, acting as an "eddy desert" with significantly less mesoscale variability. Our analyses show that these distinct regimes are primarily driven by the difference in water column properties between these two regions: the upper layer is significantly thicker in the south, compared to the north. We finally discuss the potential implications for the biological productivity in these two distinct regimes .

2 Data and methods

2.1 T/S properties around Iceland

To analyze the thermohaline properties of the ocean around Iceland, we utilize the COriolis Ocean Dataset for Reanalysis product (hereafter CORA, Szekely et al., 2019). It is a global gridded dataset of *in situ* temperature and salinity measurements from autonomous platforms (Argo profilers, fixed moorings, gliders, drifters, sea mammals) and research or opportunity vessels (CTDs, XBTs, ferrybox). The dataset provides monthly temperature (T) and salinity (S) profiles at a $0.5° \times 0.5°$ resolution over the period 1960–2023. We restrained our analysis to the 2000-2023 period to maximize the number of autonomous floats representation in the dataset.

2.2 Normal vertical mode decomposition

To assess the impact of stratification on ocean dynamics, an advanced approach involves decomposing the ocean's vertical structure into normal dynamical modes. This method allows for the separation of the water column into different depth-dependent modes that capture the full extent of stratification influences on the flow (Vallis, 2017). The dynamical regimes discussed here, *i.e.,* the mesoscale either north or south of Iceland, are characterized by a relatively small Rossby number (Ro) and timescales longer than a day. In this case, the ocean can be fairly well described by the continuously stratified Quasi-Geostrophy (QG) on an f-plane. It is formulated as the material conservation of the QG Potential Vorticity Q_{qg} (Vallis, 2017) as

$$\left[\partial_t + \mathcal{J}(\Psi, \cdot)\right] Q_{\mathrm{qg}} = 0, \tag{1}$$

where

$$Q_{\mathrm{qg}} = \nabla^2 \Psi + \frac{\partial}{\partial_z}\Big(\frac{f_0^2}{N^2}\frac{\partial}{\partial_z}\Psi\Big). \tag{2}$$

$\Psi(x, y, z, t)$ is the scalar 3D streamfunction, $\mathcal{J}$ is the Jacobian operator, f_0 the local Coriolis frequency, N the Brunt–Väisälä frequency, and x, y, z, the zonal, meridional, and vertical coordinates, respectively. The water-column dynamics are therefore intrinsically linked to the stratification of the water column N, through the so-called *stretching term* (the last term on the right-hand side in Eq. (2)). This stretching term can be decomposed into vertical dynamical modes (Gill, 1982) by projecting the streamfunction over normal modes of vertical structure $h_n(z)$ as

$$\Psi(x, y, z, t) = \sum_{n=0}^{+\infty} \psi_n(x, y, t) h_n(z), \tag{3}$$

and solving the eigenvalue problem

$$\frac{\partial}{\partial_z}\Big(\frac{1}{N^2}\frac{\partial}{\partial_z}h_n\Big) + \frac{1}{c_n^2}h_n = 0, \tag{4}$$

where c_n are the eigenvalues of the n^{th} vertical mode, which is linked to the deformation radius λ_n of each mode by $\lambda_n = c_n^2/|f_0|$. We hereafter define $\lambda_1 = R_D$, as the first baroclinic deformation radius (Chelton et al., 1998)). The modal decomposition is performed using the Python Dedalus library, with the same boundary condition as presented in Tedesco et al. (2022). This gives an estimate of h_n and λ_n for $0 \leq n \leq 10$.

This method is applied in our area of interest using the CORA dataset (see section 2.1), the T/S measurements from Argo float #4903532 (see section 2.6), and *in situ* T/S measurements from two particular repeated stations north of Iceland (blue and red crosses in Fig. 3a) over the 1990-2018 period.

2.3 Quasi-Geostrophic idealized simulations of forced turbulence

We design idealized simulations that simulate the mesoscale oceanic dynamics north and south of Iceland. There, the flow mainly consists of a turbulent flow (Villas Bôas et al., 2022), with baroclinic instability (BCI) as its primary source of energy (Callies et al., 2016). It can mainly be represented by the barotropic and first baroclinic components (*i.e.,* truncate Eq. (4) to $n = 0$ and $n = 1$, a 2-layer ocean, see Flierl, 1978). In these conditions, BCI can occur if the meridional PV gradients change sign between the surface and the bottom layer (Pedlosky, 2013), which is always the case on an f-plane if there exists a baroclinic component. The BCI eventually generates eddies of typical size πR_D (Vallis, 2017) thus defining the so-called mesoscale. The accuracy of considering only the first two modes was confirmed by use of the ECCO re-analysis (Fukumori et al., 2021); specifically, the RMSE between the current reconstruction from the first two modes and the real current is less than 10^{-3} in the open ocean in our area of interest (not shown here).

With a mean baroclinic zonal flow $\mathbf{U} = (U, -U)$, Eq. (1), can be re-written in a non-dimensionalized, 2-layer form as

$$\partial_t q_i + \mathcal{J}(\psi_i, q_i) \pm \partial_x q_i \mp F_i \partial_x \psi_i = 0, \tag{5}$$

for $i = 1, 2$ the upper and bottom layers, respectively. Where ψ_i is the streamfunction anomaly and q_i is the potential vorticity anomaly. Let's assume that the surface layer is in the rigid lid approximation and the bottom layer has no bottom friction, whose respective thicknesses are h_1 and h_2, thus defining the aspect ratio $\delta = h_1/h_2$, $F_1 = 1/(1+\delta)$, and $F_2 = \delta/(1+\delta)$. All quantities are non-dimensionalized such that $x, y \sim R_D$, $u, v \sim U$, and $t \sim R_D/U$. In this framework, the only parameters that vary are U, R_D, and δ.

We integrate these equations in a doubly periodic domain, on a 256×256 points grid, with timesteps adjusted to respect the CFL criterion. Following the formulation of Callies et al. (2016), we add dissipation terms to the right-hand side of the equations as

$$\partial_t q_i + \mathcal{J}(\psi_i, q_i) \pm \partial_x q_i \mp F_i \partial_x \psi_i = r\nabla^{-2} q_i - \nu(-\nabla^2)^n q_i. \tag{6}$$

Small scales are damped through hyperviscosity of order $n = 10$ coefficient ν, and large scales through hypoviscosity coefficient r. These later parameters are chosen to be the same in all simulations, and to be the smallest for the simulations to be at equilibrium after the turbulence has set up. They are similar to the values used in de Marez & Callies (2025). All quantities are re-dimensionalized after running the model, and we set $U = 0.04\,\mathrm{m\,s^{-1}}$ and $R_D = 15$ km in all simulations. Note that we choose to focus on the open ocean dynamics, thus, the doubly periodic domain allows to eliminate spurious boundary effects and it let eddies evolve freely. As the result, the simulations do not capture shelf-break and coastal processes. This approach is a well-established method for studying open-ocean mesoscale dynamics (see the literature of vortex studies since McWilliams & Flierl, 1979).

2.4 SWOT data and spectral analysis

We leverage newly released satellite data from the Surface Water and Ocean Topography (SWOT, see some background in *e.g.,* Morrow et al., 2019) program, a collaborative effort between NASA and CNES launched in late 2022, to unveil unprecedented details of surface mesoscale turbulence in the ocean around Iceland. Specifically, we use the latest release (v2.0) of SWOT_L3_SSH 'Basic' product, derived from the L3 SWOT KaRIn Low rate ocean data products provided by NASA/JPL and CNES. This dataset is produced and freely distributed by the AVISO and DUACS teams as part of the DESMOS Science Team project (AVISO/DUACS, 2023). The "noise-reduced" and "raw" Sea Surface Height anomaly (SSHa), displayed on a 2-km resolution grid, are used for our analysis (see Dibarboure et al., 2023, for details on the method). We use data on the 21-day repeat orbit period, from 1st September 2023 to 31st August 2024 to cover a full seasonal cycle. Recent studies (X. Zhang et al., 2024; Z. Zhang et al., 2024; Verger-Miralles et al., 2024; Du & Jing, 2024; Damerell et al., 2025; Wang et al., 2025; Tchilibou et al., 2025; Carli et al., 2025) and ongoing personal work (in the Labrador Sea, not shown) show the SWOT's ability to resolve small eddies previously undetected in gridded products. Therefore, although a complete *in* *situ* validation is not yet available, we are confident that SWOT's resolution is sufficient to study mesoscale activity in our regions of interest around Iceland. Note that the noise-reduction process applied to the SSHa tends to reduce the overall energy, which complicates the interpretation in lower-energy regions due to the noise levels (see *e.g.,* Callies & Wu, 2019). In our case of study, the conclusions remain the same when comparing the noise-reduced product with the raw product.

For each SWOT pass, whether ascending or descending, we compute wavenumber spectra. The study of such spectra is usually made in the study of oceanic geostrophic turbulence, to quantify the distribution of kinetic energy across spatial scales, revealing key dynamical processes such as energy cascades, dominant eddy sizes, and the relative importance of different forcing and dissipation mechanisms. The slope of the SSH wavenumber spectrum tends to vary between 4 and 5, depending on the underlying mechanisms generating the eddy field (Callies et al., 2015; Lawrence & Callies, 2022; de Marez et al., 2023). In this study, we compute these spectra in SWOT data following these steps: (1) We select a 600 km along-track window centered around a position $\mathbf{X}$ (tests confirm that the window size has minimal influence on the results). (2) The SSHa is re-interpolated onto a grid with a constant along-track spacing of 2 km. (3) We calculate the along-track wavenumber spectra for each cross-track position on the swath, excluding data from the central nadir altimeter. (4) These spectra are then averaged across the cross-track positions. This process produces one wavenumber spectrum for each position $\mathbf{X}$ along the track, with a spatial increment of 200 km and an associated date. To facilitate comparison, all wavenumber spectra are interpolated onto a fixed wavenumber grid for averaging. Area-averaged spectra are computed by aggregating the spectra corresponding to positions $\mathbf{X}$ within the specified region. It is important to note that data availability decreases during December, January, and February, as cloud cover and rain cells affect the altimetric measurements during these months.

We fit the wavenumber spectrum estimates to the empirical analyitical model

$$\mathcal{S} = \frac{A}{1 + (k/k_0)^s}, \tag{7}$$

where A is the spectral amplitude (describing the overall energetic level of the flow), s is the slope, and k_0 is the transition wavenumber. We refer the reader to de Marez et al. (2023) for details and justification about this spectral model.

2.5 Andro dataset

For the estimation of eddy kinetic energy (EKE) at depth, we used the ANDRO dataset (Ollitrault & Rannou, 2013), specifically the 2024 release of the Gridded Velocity Climatology from Deep Andro Velocities. This product provides binned statistics, in particular velocity fields and EKE at a spatial resolution of $3° \times 3°$, based on Argo float displacements at their parking depths of 1000 m.

2.6 Biogeochemical-Argo float data

We used data from five BGC-Argo floats (Roemmich et al., 2009) north and south of Iceland, to study the difference in nutrient input, and the consequent biological production, between the two regions. The Argo program (Argo, 2000) provides a global array of profiling floats that measure temperature, salinity, and pressure across the upper 2000 meters of the ocean. The BGC-Argo array further includes sensors for key biogeochemical parameters such as pH, oxygen, nitrate, particulate backscatter, or fluorescence-derived chlorophyll. They facilitate *in situ* sampling of the water column throughout the year, allowing us to get a comprehensive picture of both surface and subsurface oceanic features. All used floats sampled every 10 days, with a vertical resolution of 5 m (upper 100 m), 10 m (100-360 m), 20 m (360-400 m) and 50 m (400-2000 m). We further re-interpolated all profiles onto a regular 10- m vertical grid, see examples of vertical sections sampled by floats in Fig. S3.

The number of profiles we can use is limited because we only considered floats equipped with fluorescence, particulate backscatter, and nitrate sensors. This resulted in three floats south of Iceland and two floats north of Iceland, spanning part of the period 2013 to 2024. Only adjusted (except for particulate backscatter) and quality controlled data (excluding flags 3 and 4, see Bittig et al., 2019) were considered, from the Coriolis DAC. We use three variables: chlorophyll-a concentration, phytoplankton carbon and nutrient availability to describe the biogeochemical activity in the area.

First, we used the fluorescence-derived chlorophyll-a, CHLA, expressed in $\mathrm{mg\,m^{-3}}$. Only adjusted chlorophyll-a was used from the floats, where the fluorescence data have been converted to chlorophyll-a following a thorough quality control Schmechtig et al. (2015, 2023). Extended details about the method can be found in Xing et al. (2011); Petit et al. (2022), and about quality check on the BGC-Argo website (`https://biogeochemical-argo.org/`). Chlorophyll-a accuracy is 0.08 $\mathrm{mg\,m^{-3}}$ (Schmechtig et al., 2025), which leads to an uncertainty around 5% in our dataset.

Second, we estimated phytoplankton carbon, C_{phyto}, expressed in $\mathrm{mg\,C m^{-3}}$, based on bbp_{700} measured by the floats, following

$$C_{\text{phyto}} = 12,128\,\text{bbp}_{470} + 0.59, \tag{8}$$

where

$$\text{bbp}_{470} = \text{bbp}_{700}\left(\frac{470}{700}\right)^{-0.78}; \tag{9}$$

A more detailed explanation of the conversions can be found in Vives et al. (2024) and references therein. Uncertainties for bbp_{700} are $2\times10^{-4}\,\text{m}^{-1}$ (Bittig et al., 2019) translating to uncertainties of $< 1\%$ for C_{phyto} in our dataset.

Chlorophyll-a and C_{phyto} were vertically integrated over the upper 200 m, and used as a proxy for phytoplankton growth. We acknowledge that inferring biomass from bio-optical measurements has strong caveats and limitations, particularly when phytoplankton change their physiology to adapt to environmental stressors. Fluorescence-derived chlorophyll-a, for example, can be affected by iron stress (Schallenberg et al., 2022) and light limitation Vives et al. (2024). Similarly, particulate backscatter data, and the inferred phytoplankton carbon, are sensitive to seasonal changes and shifts in community composition (Cetinić et al., 2012; Schallenberg et al., 2019). The conclusions in this study are based on the relative differences between the floats in the two areas, using the same conversions and estimates. Additionally, the difference between our two areas of interest is larger than the uncertainties from each sensor, minimizing the interference in our results.

Third, we use nitrate measurements (expressed in µmol kg^{-1}) as a proxy for nutrient availability or uptake by phytoplankton. Nitrate measurements present high measurement errors up to a maximum of 1.27 µmol kg^{-1}.

2.7 Chlorophyll-a satellite data

We analysed daily satellite-derived surface chlorophyll-a data using the Global Ocean Colour (Copernicus-GlobColour), Bio-Geo-Chemical, L4 product (`doi.org/10.48670/moi-00281`). Timeseries are obtained by taking the median north and south of Iceland (in areas shown in Fig. 1).

3 Results

3.1 On the stratification differences around Iceland

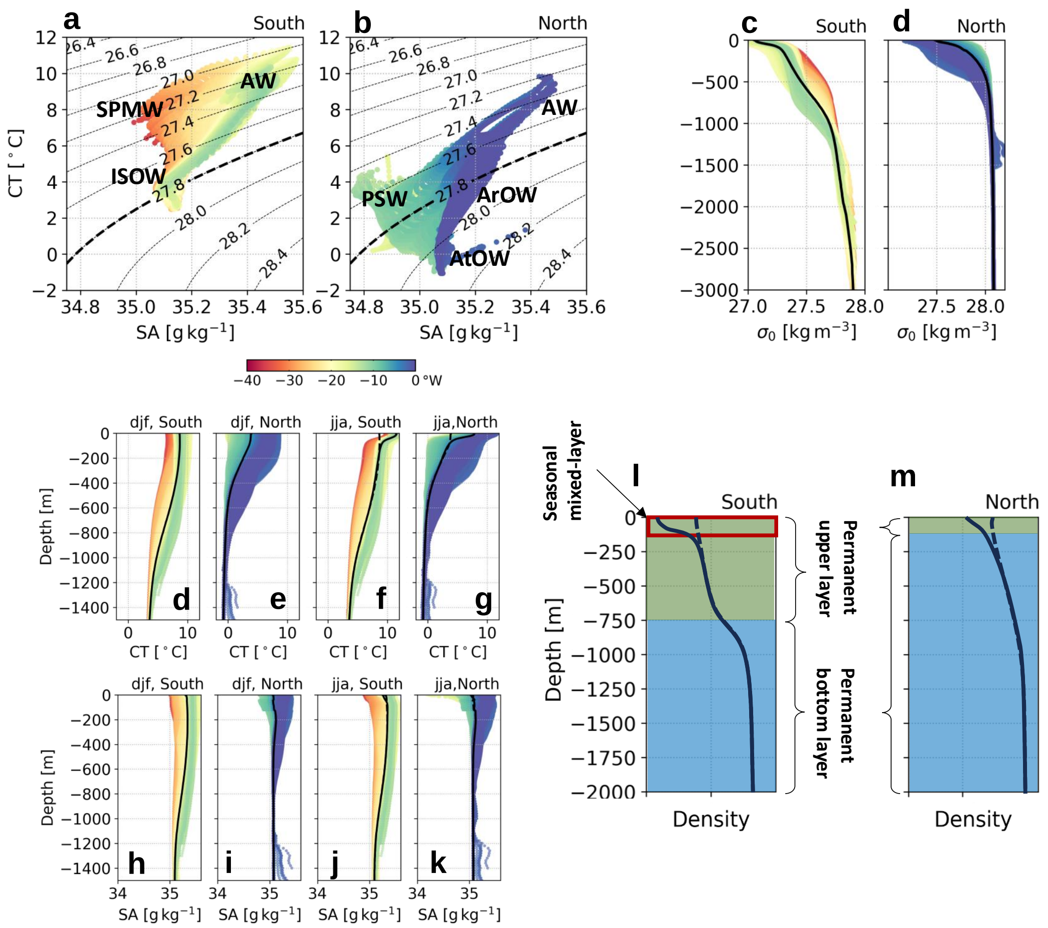

Figure 2. Stratification around Iceland from the *in situ* CORA dataset. (a, resp. b) Yearly averaged T-S diagram south (resp. north) of Iceland (see area definitions in Fig. 1). (c, resp. d) Yearly averaged potential density profiles south (resp. north) of Iceland; black line show the area average. (d-g, resp. h-k) Seasonal averaged profiles of temperature (resp. salinity) south and north of Iceland. (l,m) Schematics of the typical stratification profiles south and north of Iceland; solid line stands for the summer season and dashed line for winter; density gaps have been amplified for presentation purpose. The data is zonally bined to produce color code plots.

The main distinction between the regions north and south of Iceland is the contrast of water masses present in each area, see Fig. 2a,b. The southern area is dominated by warm, salty Atlantic-origin waters, and density variations are driven largely by temperature *i.e.,* an α-ocean (Carmack, 2007). The upper layer, between the surface and ~ 500 m depth, is composed of a combination of Atlantic Water (AW) and Subpolar Mode Water (SPMW), with more of SPMW in the west of the basin; below these, the Iceland Scotland Overflow Water (ISOW) dominates, see Fig. 2a. In contrast, in the north, water masses are largely of polar origin, with significant freshwater input from sea ice melt. Consequently, density is primarily controlled by salinity, *i.e.*, a β-ocean (Carmack, 2007). The upper layer, between the surface and ~ 100 m depth, contains mainly fresh and cold Polar Surface Water (PSW) in the west of the basin, and warm and salty AW in the east of the basin; Arctic Overflow Water (ArOW) and Atlantic Overflow Water (AtOW) are found just below, see Fig. 2b. Given the strong difference between the northern and southern water-mass properties, the stratification of the water column therefore strongly differ, see Fig. 2c-k. During winter, both areas have (1) a surface layer, (hereafter called *upper layer* and represented in green in Fig. 2l,m), and (2) an homogeneous bottom layer (represented in blue in Fig. 2l,m). During summer, a seasonal mixed-layer appears in the south due to the increased surface temperature, while in the north fresh meltwater enhances the density difference between the top and the base of the upper layer but does not impact its thickness.

The northern and southern stratification profiles are primarily distinguished by the difference in the thickness of the upper layer: it is deeper in the south than in the north, see "green layers" in Fig. 2l,m. South of Iceland, classical methods for calculating the mixed layer depth, such as temperature or density threshold approaches fail in the summertime due to the additional thin seasonal mixed-layer (see red box in Fig. 2l), and therefore underestimate the depth of the dynamically relevant surface layer (de Boyer Montégut et al., 2004). A more advanced approach involves decomposing the ocean's vertical structure into normal dynamical modes. This method allows for the separation of the water column into different depth-dependent modes that capture the full extent of stratification influences on the flow, see section 2.2 and *e.g.,* Vallis (2017).

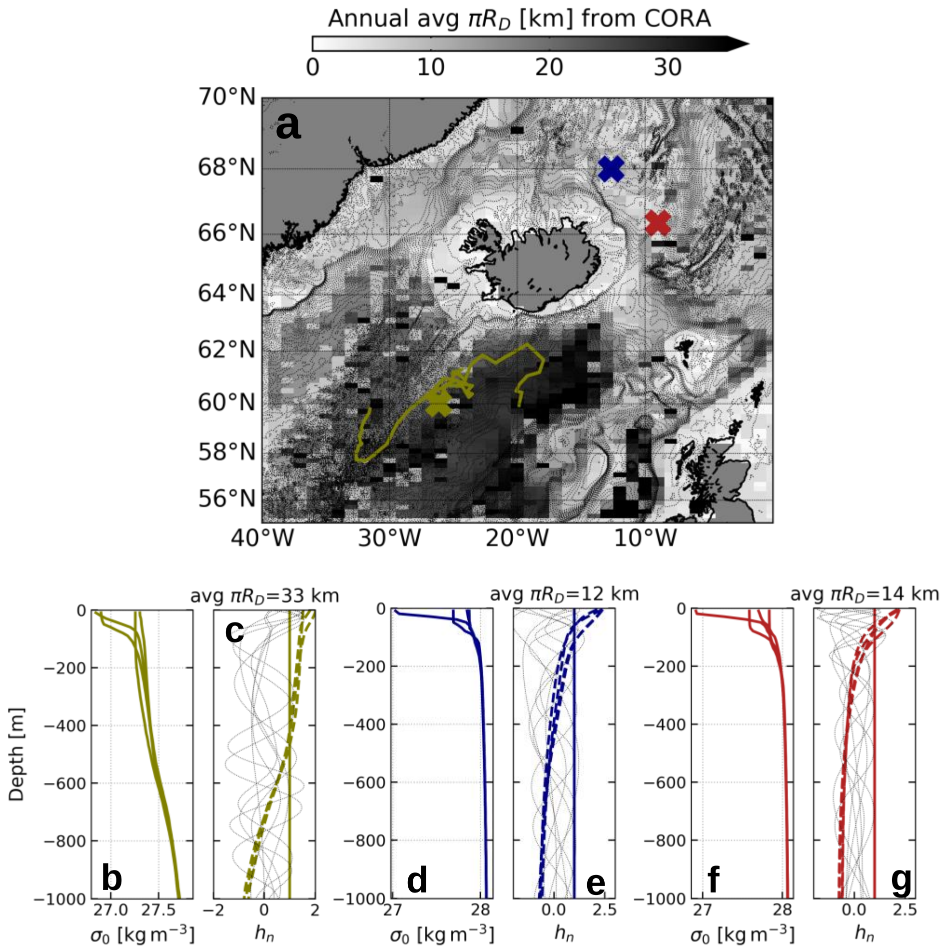

Figure 3. (a) Annual average size of mesoscale eddies πR_D from *in situ* CORA dataset, obtained by solving the normal mode equation (4), it is solely based on vertical profiles and is not affected by the resolution of the CORA product; colored crosses show the average locations where profiles of panels b-g were collected at. Yellow line recalls the trajectory of Argo float # 4903532. (b, d, f) Average potential density south of Iceland in Argo float # 4903532, in the in situ station marked with a blue cross, and with a red cross , respectively. (c, e, g) Dynamical modes obtained from profiles in panels (b, d,f) ; solid color line shows mode 0, dashed color lines shows mode 1, thin lines show modes from 2 to 10. In b-g panels, profiles are averages for each of the four seasons.

One of the key quantities obtained from this decomposition is the first baroclinic deformation radius R_D, which represents the horizontal scale at which rotational effects balance pressure gradient forces in a stratified fluid. R_D north of Iceland is less than half the value of R_D south of Iceland, with a clear delimitation made by the Greenland-Scotland ridge, see Fig. 3a. The modal decomposition further emphasizes the fact that in the south, the average stratification consists of an homogeneous upper layer about 500 m deep, independently of the season; this leads to a very deep reaching mode 1, and therefore an average value of deformation radius $R_D \sim 10$ km, Fig. 3b,c. The seasonal mixed-layer that appears in summer only impacts higher modes (see similarity of mode 1 profiles in Fig. 3c). Conversely, in the north, the stratification consists of a thin upper layer, about 100 m deep, with increased density gradients during summer, see Fig. 3d,f. The mode 1 therefore reflects the shallow upper layer, and the deformation radius $R_D \sim 5$ km, see Fig. 3e,g. Our results show that the difference in water column properties north and south of Iceland have the effect to divide by ~ 2 the value of R_D north or south of Iceland. We demonstrate in the next section how this reduced upper layer thickness and deformation radius impact the energetics of the flow around Iceland.

3.2 Dynamical regimes around Iceland

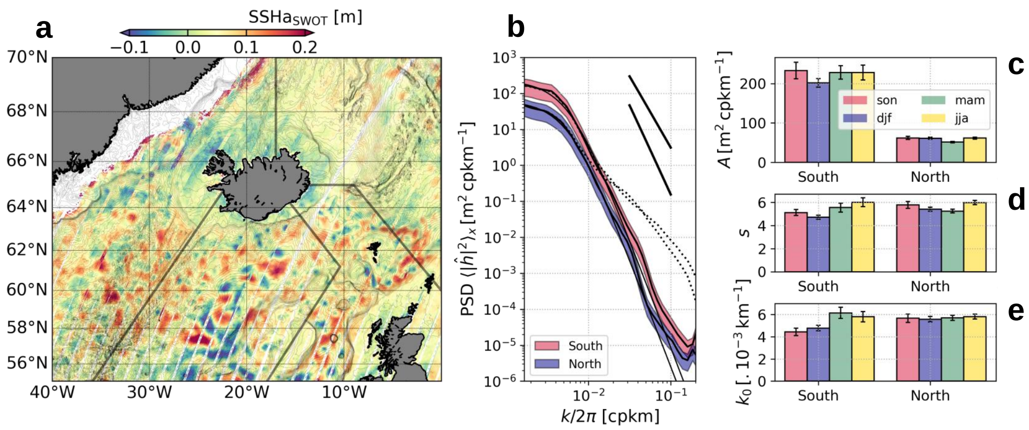

Figure 4. The surface turbulence around Iceland observed from satellite. (a) Noise-reduced SSHa from SWOT's cycle 15 (8th to 28th May 2024) descending passes. (b) Average wavenumber spectra South and North of Iceland for the month of May; solid lines show the average spectra and its fit for the noise-reduced SSHa; color envelopes show the estimated error on the average spectra; dashed line shows the average spectra using the raw SSHa; bold lines show slopes of k^{-4} and k^{-5}. (c,d,e) Amplitude, slope, and transition wavenumber for fits (see Eq. (7)) done over seasonal averaged spectra using noiseless SSHa.

Newly released SWOT altimetric data, spanning a full seasonal cycle, reveal a striking contrast in surface turbulence around Iceland: the ocean north of Iceland is significantly less energetic than the ocean to the south, see Fig. 4a. The 2-km resolution dataset provided by the SWOT (see section 2.4) enables for the first time a detailed study of turbulence in places where classical altimetry used to fail in resolving mesoscale motions (*e.g.,* north of Iceland, where the deformation radius is small). South of Iceland, the circulation is dominated by multiple intense—mostly anticyclonic—eddies, with SSHa reaching amplitudes of $\mathcal{O}(30)$ cm and sizes of $\mathcal{O}(50)$ km. In contrast, north of Iceland, SSHa rarely exceed $\mathcal{O}(10)$ cm, signifying a notably quieter ocean compared to the south and much of to the global ocean.

To quantify these energetic differences, we computed the wavenumber spectrum of the balanced motions from SSHa, using the methodology described in section 2.4. As shown in Fig. 4b, while the spectral shapes north and south of Iceland are similar, the amplitude is considerably lower in the north. Fitting the wavenumber spectrum to the model of Eq. (7) yields satisfactory results for the noise-reduced data (Fig. 4b). The spectral parameters (A, s, and k_0) display no significant seasonal variation (Fig. 4c,d,e). The spectral amplitude south of Iceland is more than double that of the north (Fig. 4c). The slope of the spectrum is around $s = 5$ (Fig. 4d), in close agreement with theoretical estimates and prior analyses (Callies et al., 2015; Lawrence & Callies, 2022; de Marez et al., 2023). Independent estimates from a high-resolution regional numerical simulation (see Fig. S1) corroborate these findings: the turbulence north of Iceland is intrinsically less energetic than that in the south. Thus, while the southern region of Iceland is characterized by intense turbulent activity, the northern region is identified as an ”eddy desert”. To ensure this observation is not biased by seasonal variability, we analyzed SWOT data across all available cycles from August 2023 to January 2025. The consistency of spectral parameters throughout the year (Fig. 4c,d,e), as well as the persistent contrast in mesoscale activity between the north and south of Iceland (not shown), confirm the robustness of our findings.

Interestingly, the physiographic characteristics of the two basins are similar: (1) both consist of deep basins (approximately > 2000 m) enclosed by sharp bathymetric features; (2) the surface forcings, including surface heat flux and wind stress, are comparable (see Fig. S2). The only difference between the north and the south is, therefore, stratification.

Idealized simulations of forced turbulence with either a shallow or a deep surface layer (*i.e.,* different aspect ratio δ, see section 2.3) allow us to model these two distinct stratification regimes. All simulations performed follow the same scenario. The energy is injected *via* BCI of the mean current because the meridional gradients of potential vorticity for the two layers have opposite signs. The growth rate of the instability is maximum at a scale of ~ 50 km $\sim \pi R_D$ km, with a value of 0.05-0.1 days^{-1} (Fig. 5a). This leads to an exponential increase of Kinetic Energy (KE) during the first months of the simulation, see Fig. 5b. Energy subsequently cascades toward larger scales, and it is dissipated at the domain scale

($\sim$ 500 km) by hypoviscosity. After a few simulated months, the KE reaches an equilibrium that lasts throughout the entire simulation (here ten years, see Fig. 5b). This represents a forced turbulence flow, with a typical wavenumber spectrum slope of 5 (computed during this equilibrium state, see Fig. 5c,e-j). This value is similar to our SWOT estimates. Strikingly, the energy content of the turbulence increases along with δ, see Fig. 5d. BCI converts the potential energy of the flow, stocked in the surface layer, into eddy kinetic energy. Therefore, the smaller δ, the smaller available potential energy, and the weaker turbulence.

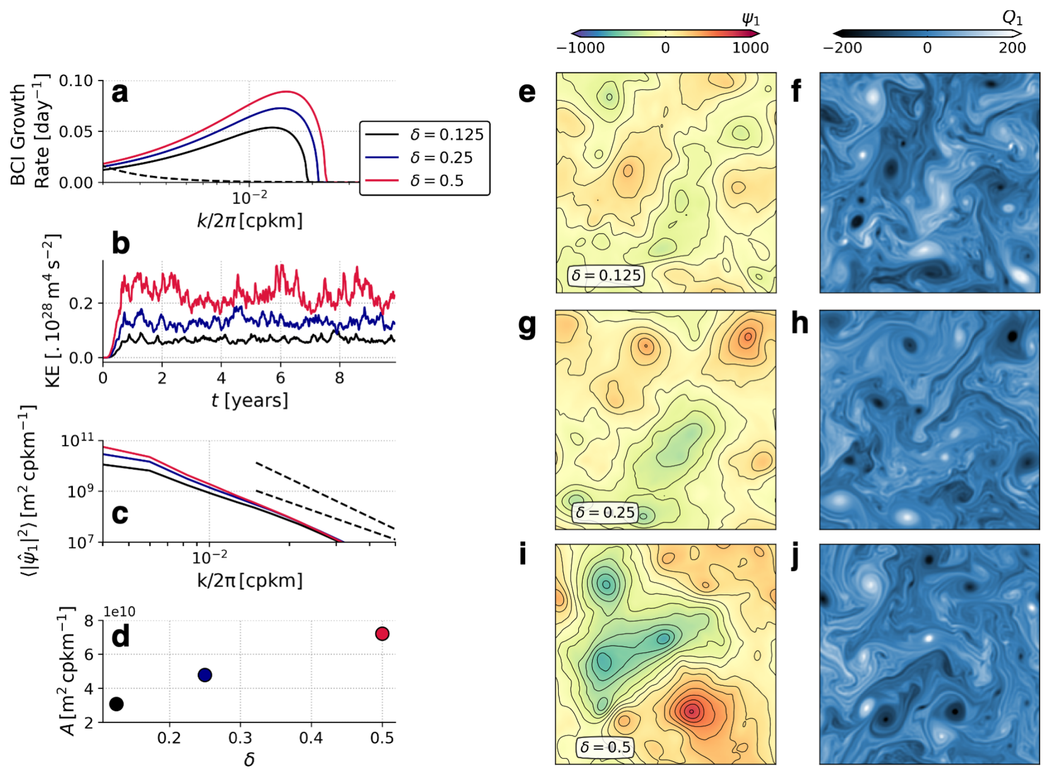

Figure 5. Results from idealized numerical simulations of forced quasi-geostrophic turbulence. (a) Growth rate of the most unstable mode for the primary BCI following linear stability calculation; dashed line shows the damping rate from hypoviscosity. (b) Surface integrated Kinetic Energy evolution in the surface layer of the QG simulation. (c) Surface streamfunction marginal wavenumber spectra; dashed lines show spectrum slopes of 4 and 5. (d) Spectral amplitude (from fits of Eq. (7) over wavenumber spectra of panel c) as a function of δ. The colors in panels a,b,c,d represent the value of δ. (e,g,i) Snapshot of surface streamfunction, equivalent to the SSH (in adimensionalized unit) for the different values of δ. (f,h,j) Snapshot of surface potential vorticity (in adimensionalized unit) for the different values of δ. In panels e-j, the domain size is 500 km.

In a nutshell, these simulations explain why the flow is so calm north of Iceland: very little potential energy is available to be converted to kinetic energy through BCI, and therefore turbulence is weak. The SSHa measured by SWOT (Fig. 4a) can be compared to the surface streamfunction in simulations (Fig. 5e,g,i). With small δ (Fig. 5e), eddies are weaker than with larger δ (Fig. 5i), analogously than the north and south of Iceland. These conclusions rely on the open-ocean mesoscale dynamics hypothesis. We cannot exclude the possibility that boundary and shelf-break processes (*e.g.,* Kelvin waves, topographic Rossby waves, upwelling, etc.) play a role in the observed regional variability (Wise et al., 2024). Further investigation, particularly with dedicated *in situ* observations and numerical model analysis, would be necessary to fully assess their potential role. Also, it is worth mentioning that there exists an interplay between the turbulent motions and the upper layer formation. As turbulence develops, eddies promote vertical motions within the upper ocean. This intensified mixing further impact the stratification set by surface heat fluxes, solar heating and other air-sea interactions, allowing the upper layer to thicken (Klein & Lapeyre, 2009).

3.3 Phenomenology of oceanic currents north and south of Iceland

In the ocean, except where large western boundary currents are present, mesoscale eddies, are the primary contributors to the surface-intensified turbulence (see *e.g.,* Z. Zhang et al., 2014) as observed by SWOT altimetry (and realistic simulations). Usually, these structures can be observed and statistically analyzed using eddy detection in gridded altimetry products (see *e.g.,* Laxenaire et al., 2018; Ernst et al., 2023). However, the reduced deformation radius north of Iceland (Fig. 3) complicates this approach and makes the interpretation of the eddy detection results very challenging. To better understand the mesoscale dynamics around Iceland, we use *in situ* data from Argo floats. They further confirm the two distinct regimes identified in the precedent section.

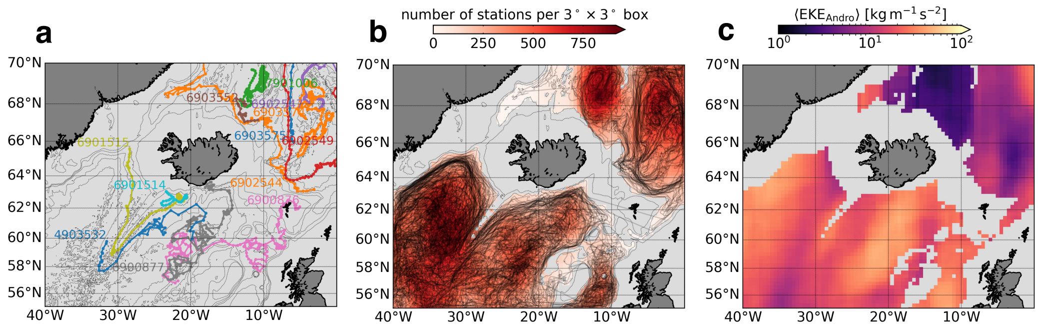

Figure 6. (a) Trajectories of selected Argo floats in the area of interest. (b) Trajectories of Argo floats used in the ANDRO dataset, and the number of stations used to compute the EKE in 3° × 3° bins. (c) Binned average of Eddy Kinetic Energy at 1000 m depth from Argo displacement.

South of Iceland, dynamics are primarily driven by deep-reaching mesoscale eddies in the middle of the Iceland Basin. For instance, floats #6900877 and #6900876, in the southern region, are trapped by eddies that extend to their 1000-m parking depth (Fig. 6a). More generally, the trajectories of most floats that enter the interior of the Iceland Basin appear to be advected by vortical structures, resulting in turbulent trajectories (Fig. 6b). This behavior leads to high values of EKE at 1000 m depth in this region (Fig. 6c), comparable to those found in high-energy areas such as the western boundaries of oceanic basins (de Marez et al., 2020). These findings support and align with previous studies using *in situ* data (see *e.g.,* Zhao et al., 2018b; Johnson et al., 2024). On the edges of the Iceland basin, trajectories of floats #6901515, #4903532, and #6901514, in the southern regime, highlight the presence of intense bottom currents flowing along the topography (see *e.g.,* Brakstad, Gebbie, et al., 2023; de Marez et al., 2024)

Conversely, north of Iceland, dynamics are mainly driven by weak, deep near-laminar currents. Limited *in situ* datasets from cruises are available in this area, although more Argo floats have been deployed there in more recent years (Jayne et al., 2017). The trajectories of some of these floats (Fig. 6a) reveal that they predominantly follow straight paths, as seen in the trajectories of floats #6903575 and #6902549. This characteristic is also seen in the trajectories of all Argo floats in the northern regime (Fig. 6b). Also, the distance between sampling stations—with 10-day intervals—is small, see floats #7901006 (in green), and #6903552 (in brown). This results in EKE values at 1000 m depth that are approximately one order of magnitude weaker than those observed south of Iceland (Fig. 6c).

4 Discussion

4.1 Unveiling the mesoscale dynamics north of Iceland

Our study provides a new perspective on oceanic circulation around Iceland. Previous studies have focused primarily on the Iceland Basin and their role in heat transport (Zhao et al., 2018a, 2018b), while turbulence in the north remained largely undocumented due to observational limitations (Beaird et al., 2013). Here, high-resolution SWOT altimetry dataset allowed us to provide the first detailed characterization of mesoscale turbulence north of Iceland. We show that the ocean north of Iceland is significantly less energetic than its southern counterpart, in contrast to the south, where strong mesoscale eddies dominate the flow.

These results challenge the assumption that bathymetry or surface forcing alone determine regional differences in ocean dynamics. Instead, we show that the primary driver of this difference is stratification. South of Iceland, a thick upper layer ($\sim$500 m) supports strong baroclinic instability, allowing eddies to grow and sustain energetic turbulence. In contrast, the north has a much shallower upper layer ($\sim$100 m), limiting the energy available for eddy formation. These findings contribute to broader research on subpolar ocean variability (Brakstad, Gebbie, et al., 2023) and underscore the importance of high-resolution observations in improving our understanding of mesoscale dynamics in previously unresolved regions. Future work combining SWOT data with additional *in situ* measurements and high-resolution numerical modeling will be essential to further investigate the mesoscale variability at high latitude.

4.2 Implications for ocean biogeochemistry around Iceland

Mesoscale eddies influence ocean biogeochemistry through the water column globally (Su et al., 2021; Cornec et al., 2021). Eddies facilitate upwelling of nutrients (Patel et al., 2020) and carbon flux (Moreau et al., 2017). For instance, cyclonic eddies create optimal conditions for phytoplankton growth in deeper layers when nutrients are all consumed at the surface, creating subsurface or deep chlorophyll-a maxima (Cornec et al., 2021). The North Atlantic is known for being a highly productive area during spring (Westberry et al., 2016). Particularly, in the Iceland Basin, studies using remote sensing (Siegel et al., 2002), and cruise data (Poulton et al., 2010), show highly productive blooms during the growing season. Although cruise data for the Iceland Sea are more limited, they suggest it to be less productive (Jeansson et al., 2015; Richardson & Bendtsen, 2021), thus suggesting a higher primary productivity in the south than in the north of Iceland (Thórdardóttir, 1986; Zhai et al., 2012; Cerfonteyn et al., 2023).

We test the hypothesis of the link between mesoscale activity and biological production by analyzing chlorophyll-a and phytoplankton carbon data from BGC-Argo floats (see section 2.6). The timeseries suggest a clear difference in phytoplankton growth between the northern and the southern regions. We observe more prolonged, and overall larger, phytoplankton blooms in the south compared to the north (see Fig. 7).

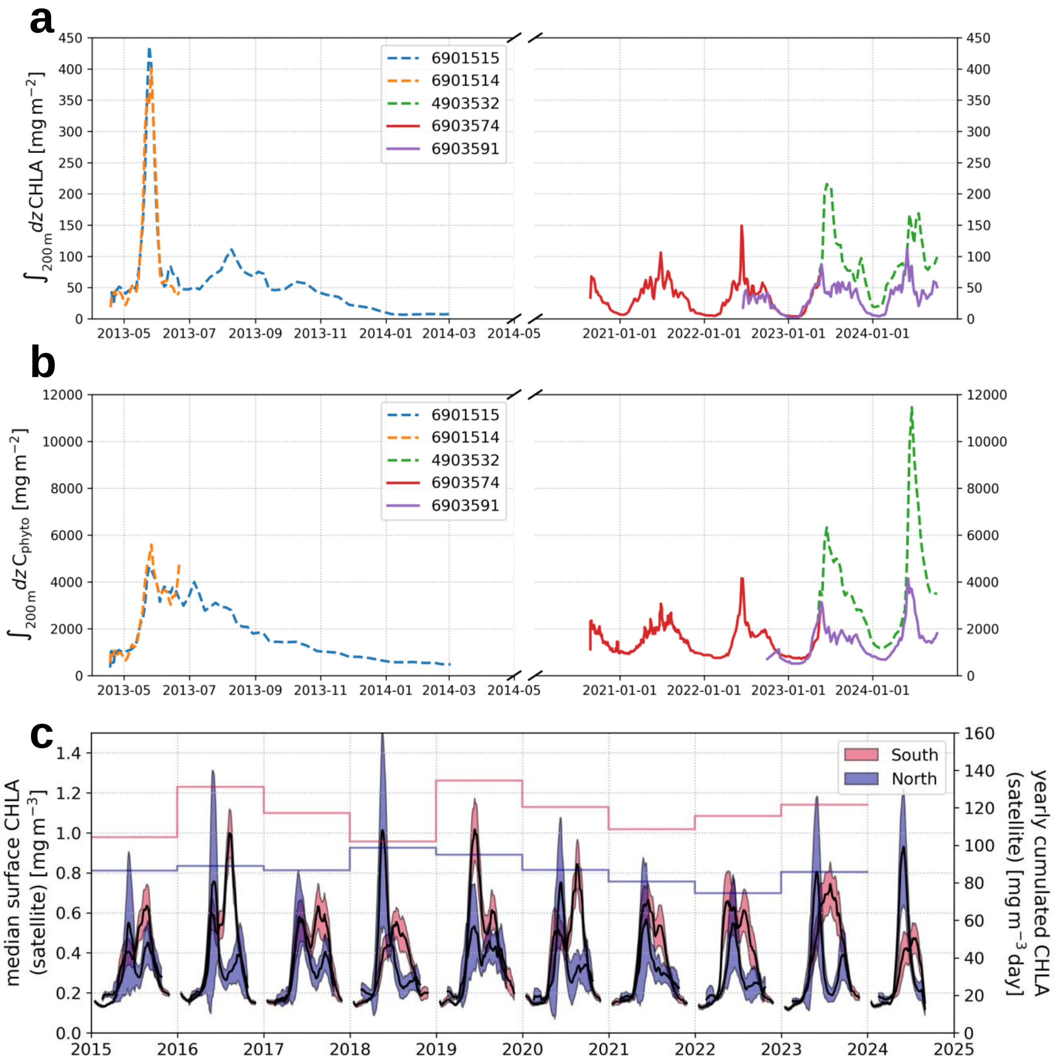

Figure 7. (a, resp. b) Timeseries of chlorophyll-a (resp. phytoplankton carbon) integrated in the upper 200 m from BGC-Argo floats; solid (resp. dashed) lines are for floats located north (resp. south) of Iceland. (c) Median chlorophyll-a north and south of Iceland from satellite measurements in a 10-year period (see section 2.7); envelopes show the standard deviation in the areas; bar plot (right y-axis) shows the cumulated median SSH over each year.

The northern region has lower concentrations of chlorophyll-a and phytoplankton carbon compared to the southern region, particularly during the phytoplankton growing season in 2023 and 2024 (*i.e.,* April to June, Fig. 7a,b). In 2024, for example, where there are two floats sampling at the same time, the southern regime shows more than double of chlorophyll-a concentrations (200 mg m^{-2}) in the water column compared to the north (50 mg m^{-2}). However, fluorescence-derived chlorophyll-a can sometimes be biased due to iron stress (Schallenberg et al., 2022) and light limitation of phytoplankton growth (Westberry et al., 2008). We therefore use phytoplankton carbon, as an additional and more reliable proxy of phytoplankton production at high latitudes (Vives et al., 2024). The difference in phytoplankton carbon is even greater between the two regimes, where values are up to 10,000 mg C m^{-2} higher in the south compared to the north.

While the temporal frame of these floats is small, a decade of satellite-derived chlorophyll-a concentrations exhibits the same pattern. Blooms are longer in the southern regime. This leads to overall higher yearly integrated median surface chlorophyll-a in the south compared to the north (Fig. 7c), *i.e.,* higher production over time in the south than in the north.

Float data shows slightly higher, although not significantly, nitrate concentrations at the surface and in the upper 200 m in the northern regime compared to the south (Fig. S4). Along with the differences in productivity, this could suggest higher nutrient uptake in the southern regime, where phytoplankton are able to utilize more available nutrients to continue growing, leading to prolonged blooms. However, the Iceland Basin is known for being iron limited in the summer (Ryan-Keogh et al., 2013; Nielsdóttir et al., 2009; Moore et al., 2013), meaning that nitrate concentrations may not be representative of nutrient availability in this area.

These findings are consistent with previous long-term observations, using either satellite algorithms to derive primary production or *in situ* data, that point out the high productivity of the Iceland Basin compared to the Iceland Sea (Thórdardóttir, 1986; Zhai et al., 2012; Richardson & Bendtsen, 2021; Cerfonteyn et al., 2023). This may lead to hypothesize that the high mesoscale turbulent activity in the south ultimately affects the biogeochemical variability south of Iceland, thus explaining the difference in productivity between the north and the south. We could indeed hypothesize that the larger upper layer thicknesses and stronger mesoscale current activity at greater depths may be facilitating nutrient upwelling to the surface in the south. There, the higher upwelling of nutrients may facilitate an increase in longevity and vertical extension of blooms. On the contrary, thinner upper layer thicknesses and weaker EKE values in the north, primarily occurring at shallower depths, may be limiting nutrient supply to the surface.

As a result, phytoplankton is subjected to the surface in the northern region, where growth may be terminated promptly with the diminishment of nutrient availability earlier in the season. While consistent with our observations, these interpretations remain speculative and require further data for confirmation. Our study serves as a first step toward unveiling the coupling between physical and biogeochemical processes around Iceland, highlighting the need for future targeted observations and modeling.

4.3 Future Changes in a warming climate

Recent studies suggest that global warming is significantly affecting the upper ocean stratification around Iceland, driven by changes in both temperature and salinity, which directly influence the upper layer thickness. The region, particularly in the northeast, has warmed in the last decades (Polyakov et al., 2017; Dai et al., 2019), as the influx of warmer AW initiated a process known as "Atlantification"—where Arctic waters increasingly take on the characteristics of Atlantic conditions due to the penetration of warmer, saltier waters. The effects of Atlantification are twofold. In northern regions, driven by the increasing intrusion of Atlantic Water, Atlantification is expected to weaken the typical upper-ocean stratification. This would promote deeper mixing, resulting in a deeper mixed layer. In contrast, south of Iceland, surface warming will strengthen upper-ocean stratification, limiting vertical mixing to shallower depths and likely leading to a shallower mixed layer depth. These changes may have significant impacts on dynamical biogeochemical activity in the region. A thicker upper layer in the northern areas would allow for a more turbulent ocean with greater vertical mixing, which could enhance nutrient availability, supporting biological productivity at the surface if other conditions are optimal for phytoplankton growth. However, in the southern region, where the upper layer is expected to become shallower, eddy generation *via* BCI may decrease, thus limiting nutrient upwelling from deeper waters. This could reduce primary productivity, particularly during the growing season, as essential nutrients for phytoplankton growth become less accessible. As the southern region is observed to be more productive, warming-derived changes might have consequences for the biological carbon pump. Overall, this might shift northward the primary production patterns, and therefore perturb the entire marine food web around Iceland.

Open Research Section

CORA data, can be downloaded from the Copernicus Marine Service at `https://data.marine.copernicu` `.eu/product/INSITU_GLO_PHY_TS_OA_MY_013_052/`. BGC-Argo float data are available on the Ifremer Argo Data Assembly Center at `https://data-argo.ifremer.fr/dac`. *in situ* data from the two stations north of Iceland is provided by the SeaDataNet Pan-European infrastructure for ocean and marine data management (`https://www.seadatanet.org`), and can be downloaded as part of the SDC_ARC_DATA_TS_V2 dataset and the Norwegian Marine Data Center (Brakstad, Våge, et al., 2023). The measurement were made during the observational program of the Icelandic Marine and Freshwater Research Institute. QG numerical simulation code is available at `https://github.com/joernc/QGModel`. SWOT data can be downloaded on AVISO website `https://www.aviso.altimetry.fr/en/my-aviso-plus.html`. ANDRO dataset is available through the SEANOE platform and is part of the comprehensive ANDRO Argo-based velocity product managed by Coriolis, at `https://www.seanoe.org/data/00360/47077/`. Satellite measurements of chlorophyll-a can be downloaded using E.U. Copernicus Marine Service Information at `https://data.marine.copernicus.eu/product/OCEANCOLOUR_GLO_BGC_L4_MY_009_104/`. Scripts to reproduce results of this paper can be obtained online (de Marez, 2024).

Acknowledgments

C.d.M. was supported by a Queen Margrethe II´s and Vigdís Finnbogadóttir's Interdisciplinary Research Centre on Ocean, Climate and Society (ROCS) postdoctoral fellowship. A.R.A. was supported by ROCS. C.R.V. was supported by the Centre for Glacial Rock Flour Research, Globe Institute, University of Copenhagen. We thoroughly thank E.C. for her precious help finding, analyzing, and downloading BGC-Argo data.

References

Argo, G. (2000). Argo float data and metadata from global data assembly centre (argo gdac). *Seanoe*, *2000*(42182).

AVISO/DUACS. (2023). SWOT Level-3 SSH Basic (v0.3) [Data set]. doi: 0.24400/527896/A01-2023.017

Bashmachnikov, I., Raj, R., Golubkin, P., & Kozlov, I. (2023). Heat transport by mesoscale eddies in the norwegian and greenland seas. *Journal of Geophysical Research: Oceans*, *128*(2), e2022JC018987.

Beaird, N., Rhines, P., & Eriksen, C. (2013). Overflow waters at the Iceland–Faroe Ridge observed in multiyear seaglider surveys. *Journal of Physical Oceanography*, *43*(11), 2334–2351.

Bindoff, N. L., Cheung, W. W., Kairo, J. G., Arístegui, J., Guinder, V. A., Hallberg, R., ... others (2019). Changing ocean, marine ecosystems, and dependent communities.

Bittig, H. C., Maurer, T. L., Plant, J. N., Schmechtig, C., Wong, A. P., Claustre, H., ... others (2019). A BGC-Argo guide: Planning, deployment, data handling and usage. *Frontiers in marine science*, *6*, 502.

Bosse, A., Fer, I., Lilly, J. M., & Søiland, H. (2019). Dynamical controls on the longevity of a non-linear vortex: The case of the Lofoten Basin Eddy. *Scientific reports*, *9*(1), 13448.

Brakstad, A., Gebbie, G., Våge, K., Jeansson, E., & Ólafsdóttir, S. R. (2023). Formation and pathways of dense water in the Nordic Seas based on a regional inversion. *Progress in Oceanography*, *212*, 102981.

Brakstad, A., Våge, K., Ólafsdóttir, S. R., Jeansson, E., & Gebbie, G. (2023). Hydrographic and geochemical observations in the nordic seas between 1950 and 2019. , 102981. doi: 10.21335/NMDC-1271328906

Buckley, M. W., & Marshall, J. (2016). Observations, inferences, and mechanisms of the Atlantic Meridional Overturning Circulation: A review. *Reviews of Geophysics*, *54*(1), 5–63.

Callies, J., Ferrari, R., Klymak, J. M., & Gula, J. (2015, November). Seasonality in submesoscale turbulence. *Nature Communications*, *6*(1), 6862.

Callies, J., Flierl, G., Ferrari, R., & Fox-Kemper, B. (2016). The role of mixed-layer instabilities in submesoscale turbulence. *Journal of Fluid Mechanics*, *788*, 5–41. doi: 10.1017/jfm.2015.700

Callies, J., & Wu, W. (2019, September). Some Expectations for Submesoscale Sea Surface Height Variance Spectra. *Journal of Physical Oceanography*, *49*(9), 2271–2289.

Carli, E., Tranchant, Y., Siegelman, L., Le Guillou, F., Morrow, R. A., Ballarotta, M., & Vergara, O. (2025). Small-scale eddy diagnostics around the Southern Ocean Polar Front with SWOT. *Authorea Preprints*.

Carmack, E. C. (2007). The alpha/beta ocean distinction: A perspective on freshwater fluxes, convection, nutrients and productivity in high-latitude seas. *Deep Sea Research Part II: Topical Studies in Oceanography*, *54*(23-26), 2578–2598.

Casanova-Masjoan, M., Pérez-Hernández, M. D., Pickart, R. S., Valdimarsson, H., Ólafsdóttir, S., Macrander, A., ... others (2020). Along-stream, seasonal, and interannual variability of the North Icelandic Irminger Current and East Icelandic Current around Iceland. *Journal of Geophysical Research: Oceans*, *125*(9), e2020JC016283.

Cerfonteyn, M., Groben, R., Vaulot, D., Gumundsson, K., Vannier, P., Pérez-Hernández, M. D., & Marteinsson, V. . (2023). The distribution and diversity of eukaryotic phytoplankton in the icelandic marine environment. *Scientific Reports*, *13*(1), 8519.

Cetinić, I., Perry, M. J., Briggs, N. T., Kallin, E., D'Asaro, E. A., & Lee, C. M. (2012). Particulate organic carbon and inherent optical properties during 2008 north atlantic bloom experiment. *Journal of Geophysical Research: Oceans*, *117*(C6).

Chelton, D. B., DeSzoeke, R. A., Schlax, M. G., El Naggar, K., & Siwertz, N. (1998). Geographical variability of the first baroclinic Rossby radius of deformation. *Journal of Physical Oceanography*, *28*(3), 433–460.

Cornec, M., Laxenaire, R., Speich, S., & Claustre, H. (2021). Impact of mesoscale eddies on deep chlorophyll maxima. *Geophysical Research Letters*, *48*(15), e2021GL093470.

Dai, A., Luo, D., Song, M., & Liu, J. (2019). Arctic amplification is caused by sea-ice loss under increasing co2. *Nature communications*, *10*(1), 121.

Damerell, G. M., Bosse, A., & Fer, I. (2025). Merging of a mesoscale eddy into the Lofoten Vortex in the Norwegian Sea captured by an ocean glider and SWOT observations. *EGUsphere*, *2025*, 1–28.

de Marez, C. (2024). Functions to reproduce results in de marez et al. [Software]. Zenodo. doi: 10.5281/zenodo.14145082

de Marez, C., & Callies, J. (2025). The information contained in altimetric sea surface height frequency spectra. *Journal of Physical Oceanography*, *55*(2), 119–129.

de Marez, C., Callies, J., Haines, B., Rodriguez-Chavez, D., & Wang, J. (2023). Observational constraints on the submesoscale sea surface height variance of balanced motion. *Journal of Physical Oceanography*, *53*(5), 1221–1235.

de Marez, C., Meunier, T., Tedesco, P., L'Hégaret, P., & Carton, X. (2020). Vortex–wall interaction on the β-plane and the generation of deep submesoscale cyclones by internal Kelvin Waves–current interactions. *Geophysical & Astrophysical Fluid Dynamics*, *114*(4-5), 588–606.

de Marez, C., Ruiz-Angulo, A., & Le Corre, M. (2024). Structure of the bottom boundary current South of Iceland and spreading of deep waters by submesoscale processes. *Geophysical Research Letters*, *51*(5), e2023GL107508.

de Boyer Montégut, C., Madec, G., Fischer, A. S., Lazar, A., & Iudicone, D. (2004). Mixed layer depth over the global ocean: An examination of profile data and a profile-based climatology. *Journal of Geophysical Research: Oceans*, *109*(C12).

Dibarboure et al. (2023). *SWOT Level-3 Overview algorithms and examples.* `https://swotst.aviso.altimetry.fr/fileadmin/user_upload/SWOTST2023/postersPI/faugere_ocean_l3_PIproject.pdf`. (Poster at SWOT Science Team 2023)

Du, T., & Jing, Z. (2024). Fine-scale eddies detected by swot in the kuroshio extension. *Remote Sensing*, *16*(18), 3488.

Ernst, P. A., Subrahmanyam, B., Morel, Y., Trott, C. B., & Chaigneau, A. (2023). Subsurface Eddy Detection Optimized with Potential Vorticity from Models in the Arabian Sea. *Journal of Atmospheric and Oceanic Technology*, *40*(6), 677–700.

Flierl, G. R. (1978). Models of vertical structure and the calibration of two-layer models. *Dynamics of Atmospheres and Oceans*, *2*(4), 341–381.

Fukumori, I., Wang, O., Fenty, I., Forget, G., Heimbach, P., & Ponte, R. M. (2021, February). *Synopsis of the ECCO Central Production Global Ocean and Sea-Ice State Estimate, Version 4 Release 4* (Tech. Rep.). Zenodo. Retrieved 2022-10-25, from `https://zenodo.org/record/3765928` (Version Number: 4 Release 4) doi: 10.5281/ZENODO.3765928

Gill, A. E. (1982). *Atmosphere-Oocean dynamics* (Vol. 30). Academic press.

Godø, O. R., Samuelsen, A., Macaulay, G. J., Patel, R., Hjøllo, S. S., Horne, J., ... Johannessen, J. A. (2012). Mesoscale eddies are oases for higher trophic marine life. *PloS one*, *7*(1), e30161.

Hansen, B., & Østerhus, S. (2000). North atlantic–nordic seas exchanges. *Progress in oceanography*, *45*(2), 109–208.

Jayne, S. R., Roemmich, D., Zilberman, N., Riser, S. C., Johnson, K. S., Johnson, G. C., & Piotrowicz, S. R. (2017). The argo program: Present and future. *Oceanography*, *30*(2), 18–28.

Jeansson, E., Bellerby, R. G., Skjelvan, I., Frigstad, H., Ólafsdóttir, S. R., & Olafsson, J. (2015). Fluxes of carbon and nutrients to the iceland sea surface layer and inferred primary productivity and stoichiometry. *Biogeosciences*, *12*(3), 875–885.

Johnson, L., Siegel, D. A., Thompson, A. F., Fields, E., Erickson, Z. K., Cetinic, I., . . . others (2024). Assessment of oceanographic conditions during the north atlantic export processes in the ocean from remote sensing (exports) field campaign. *Progress in Oceanography*, *220*, 103170.

Jonsson, S., & Valdimarsson, H. (2004). A new path for the denmark strait overflow water from the iceland sea to denmark strait. *Geophysical Research Letters*, *31*(3).

Klein, P., & Lapeyre, G. (2009). The oceanic vertical pump induced by mesoscale and submesoscale turbulence. *Annual review of marine science*, *1*(1), 351–375.

Lawrence, A., & Callies, J. (2022). Seasonality and Spatial Dependence of Mesoscale and Submesoscale Ocean Currents from Along-Track Satellite Altimetry. *Journal of Physical Oceanography*(9). doi: 10.1175/JPO-D-22-0007.1

Laxenaire, R., Speich, S., Blanke, B., Chaigneau, A., Pegliasco, C., & Stegner, A. (2018). Anticyclonic eddies connecting the western boundaries of Indian and Atlantic Oceans. *Journal of Geophysical Research: Oceans*, *123*(11), 7651–7677.

Logemann, K., Ólafsson, J., Snorrason, Á., Valdimarsson, H., & Marteinsdóttir, G. (2013). The circulation of icelandic waters–a modelling study. *Ocean Science*, *9*(5), 931–955.

Mahadevan, A., D'asaro, E., Lee, C., & Perry, M. J. (2012). Eddy-driven stratification initiates north atlantic spring phytoplankton blooms. *Science*, *337*(6090), 54–58.

McGillicuddy, D. J., Anderson, L. A., Bates, N. R., Bibby, T., Buesseler, K. O., Carlson, C. A., . . . Steinberg, D. K. (2007). Eddy/Wind Interactions Stimulate Extraordinary Mid-Ocean Plankton Blooms. *Science*, *316*(5827), 1021-1026. doi: 10.1126/science.1136256

McWilliams, J. C., & Flierl, G. R. (1979). On the evolution of isolated, nonlinear vortices. *Journal of Physical Oceanography*, *9*(6), 1155–1182.

Moore, C., Mills, M., Arrigo, K., Berman-Frank, I., Bopp, L., Boyd, P., . . . others (2013). Processes and patterns of oceanic nutrient limitation. *Nature geoscience*, *6*(9), 701–710.

Moreau, S., Penna, A. D., Llort, J., Patel, R., Langlais, C., Boyd, P. W., . . . others (2017). Eddy-induced carbon transport across the Antarctic Circumpolar Current. *Global Biogeochemical Cycles*, *31*(9), 1368–1386.

Morrow, R., Fu, L.-L., Ardhuin, F., Benkiran, M., Chapron, B., Cosme, E., . . . others (2019). Global observations of fine-scale ocean surface topography with the Surface Water and Ocean Topography (SWOT) mission. *Frontiers in Marine Science*, *6*, 232.

Nielsdóttir, M. C., Moore, C. M., Sanders, R., Hinz, D. J., & Achterberg, E. P. (2009). Iron limitation of the postbloom phytoplankton communities in the iceland basin. *Global Biogeochemical Cycles*, *23*(3).

Ólafsson, J. (2003). Winter mixed layer nutrients in the irminger and iceland seas, 1990-2000.

Ollitrault, M., & Rannou, J. (2013). ANDRO: An Argo-based deep displacement dataset. *Journal of Atmospheric and Oceanic Technology*, *30*(4), 759–788.

Patel, R. S., Llort, J., Strutton, P. G., Phillips, H. E., Moreau, S., Conde Pardo, P., & Lenton, A. (2020). The biogeochemical structure of Southern Ocean mesoscale eddies. *Journal of Geophysical Research: Oceans*, *125*(8), e2020JC016115.

Pedlosky, J. (2013). *Geophysical fluid dynamics.* Springer Science & Business Media.

Petit, F., Uitz, J., Schmechtig, C., Dimier, C., Ras, J., Poteau, A., ... Claustre, H. (2022). Influence of the phytoplankton community composition on the in situ fluorescence signal: Implication for an improved estimation of the chlorophyll-a concentration from BioGeoChemical-Argo profiling floats. *Frontiers in Marine Science*, *9*, 959131.

Polyakov, I. V., Pnyushkov, A. V., Alkire, M. B., Ashik, I. M., Baumann, T. M., Carmack, E. C., ... others (2017). Greater role for atlantic inflows on sea-ice loss in the eurasian basin of the arctic ocean. *Science*, *356*(6335), 285–291.

Pörtner, H.-O., Roberts, D. C., Masson-Delmotte, V., Zhai, P., Tignor, M., Poloczanska, E., & Weyer, N. (2019). The ocean and cryosphere in a changing climate. *IPCC special report on the ocean and cryosphere in a changing climate*, *1155*.

Poulton, A. J., Charalampopoulou, A., Young, J. R., Tarran, G. A., Lucas, M. I., & Quartlya, G. D. (2010). Coccolithophore dynamics in non-bloom conditions during late summer in the central iceland basin (july-august 2007). *Limnology and Oceanography*, *55*(4), 1601–1613.

Richardson, K., & Bendtsen, J. (2021). Distinct seasonal primary production patterns in the subpolar gyre and surrounding seas. *Frontiers in Marine Science*, *8*, 785685.

Roemmich, D., Johnson, G. C., Riser, S., Davis, R., Gilson, J., Owens, W. B., ... Ignaszewski, M. (2009). The Argo Program: Observing the global ocean with profiling floats. *Oceanography*, *22*(2), 34–43.

Ruiz, S., Claret, M., Pascual, A., Olita, A., Troupin, C., Capet, A., ... others (2019). Effects of oceanic mesoscale and submesoscale frontal processes on the vertical transport of phytoplankton. *Journal of Geophysical Research: Oceans*, *124*(8), 5999–6014.

Ryan-Keogh, T. J., Macey, A. I., Nielsdóttir, M. C., Lucas, M. I., Steigenberger, S. S., Stinchcombe, M. C., ... Moore, C. M. (2013). Spatial and temporal development of phytoplankton iron stress in relation to bloom dynamics in the high-latitude north atlantic ocean. *Limnology and oceanography*, *58*(2), 533–545.

Sallée, J.-B., Pellichero, V., Akhoudas, C., Pauthenet, E., Vignes, L., Schmidtko, S., ... Kuusela, M. (2021). Summertime increases in upper-ocean stratification and mixed-layer depth. *Nature*, *591*(7851), 592–598.

Schallenberg, C., Harley, J. W., Jansen, P., Davies, D. M., & Trull, T. W. (2019). Multi-year observations of fluorescence and backscatter at the southern ocean time series (sots) shed light on two distinct seasonal bio-optical regimes. *Frontiers in Marine Science*, *6*, 595.

Schallenberg, C., Strzepek, R. F., Bestley, S., Wojtasiewicz, B., & Trull, T. W. (2022). Iron limitation drives the globally extreme fluorescence/chlorophyll ratios of the southern ocean. *Geophysical Research Letters*, *49*(12), e2021GL097616.

Schmechtig, C., Claustre, H., Poteau, A., D'Ortenzio, F., Schallenberg, C., Trull, T., & Xing, X. (2023). Manuel de contrôle qualité de la concentration en chlorophylle-a bio-argo.

Schmechtig, C., Poteau, A., Claustre, H., D'Ortenzio, F., & Boss, E. (2015). Processing bio-argo chlorophyll-a concentration at the dac level. *Version 1.0. 30 September 2015.*.

Schmechtig, C., Sauzède, R., Lemasson, P., Bretagnon, M., Pannimpullath Remanan, R., & Claustre, H. (2025). Collection of BGC-Argo single synthetic profile files with improved post processed Chlorophyll-A at the global scale.
doi: 10.17882/102324

Semper, S., Våge, K., Pickart, R. S., Jónsson, S., & Valdimarsson, H. (2022). Evolution and transformation of the north icelandic irminger current along the north iceland shelf. *Journal of Geophysical Research: Oceans*, *127*(3), e2021JC017700.

Siegel, D., Doney, S., & Yoder, J. (2002). The north atlantic spring phytoplankton bloom and sverdrup's critical depth hypothesis. *science*, *296*(5568), 730–733.

Soman, A. A., Chafik, L., & Nilsson, J. (2022). Linking coherent anticyclonic eddies in the iceland basin to decadal oceanic variability in the subpolar North Atlantic. *Journal of Geophysical Research: Oceans*, *127*(5), e2021JC018046.

Su, J., Strutton, P. G., & Schallenberg, C. (2021). The subsurface biological structure of Southern Ocean eddies revealed by BGC-Argo floats. *Journal of marine systems*, *220*, 103569.

Szekely, T., Gourrion, J., Pouliquen, S., Reverdin, G., & Merceur, F. (2019). CORA, coriolis ocean dataset for reanalysis.

Tchilibou, M., Carrere, L., Lyard, F., Ubelmann, C., Dibarboure, G., Zaron, E. D., & Arbic, B. K. (2025). Internal tides off the Amazon shelf in the western tropical Atlantic: analysis of SWOT Cal/Val mission data. *Ocean Science*, *21*(1), 325–342.

Tedesco, P., Gula, J., Penven, P., & Ménesguen, C. (2022). Mesoscale Eddy Kinetic Energy budgets and transfers between vertical modes in the Agulhas Current. *Journal of Physical Oceanography*, *52*(4), 677–704.

Thórdardóttir, T. (1986). Timing and duration of spring blooming south and southwest of iceland. In *The role of freshwater outflow in coastal marine ecosystems* (pp. 345–360). Springer.

Vallis, G. K. (2017). *Atmospheric and oceanic fluid dynamics*. Cambridge University Press.

Verger-Miralles, E., Mourre, B., Gómez-Navarro, L., Barceló-Llull, B., Casas, B., Cutolo, E., ... others (2024). SWOT enhances small-scale intrathermocline eddy detection. *Authorea Preprints*.

Villas Bôas, A. B., Lenain, L., Cornuelle, B. D., Gille, S. T., & Mazloff, M. R. (2022). A broadband view of the Sea Surface Height wavenumber spectrum. *Geophysical Research Letters*, *49*(4), e2021GL096699.

Vives, C. R., Schallenberg, C., Strutton, P. G., & Boyd, P. W. (2024). Biogeochemical-argo floats show that chlorophyll increases before carbon in the high-latitude southern ocean spring bloom. *Limnology and Oceanography Letters*, *9*(3), 172–182.

Voet, G., Waterhouse, A. F., Savage, A., Kunze, E., MacKinnon, J. A., Alford, M. H., ... Girton, J. B. (2024, December). Near-inertial energy variability in a strong mesoscale eddy field in the iceland basin. *Oceanography*, $issue_volume.Retrievedfrom$

Wang, J., Archer, M., Klein, P., & Fu, L.-L. (2025). Global Submesoscale Ocean Dynamics Unveiled by Wide-Swath Satellite Altimetry.

Westberry, T. K., Behrenfeld, M., Siegel, D., & Boss, E. (2008). Carbon-based primary productivity modeling with vertically resolved photoacclimation. *Global Biogeochemical Cycles*, *22*(2).

Westberry, T. K., Schultz, P., Behrenfeld, M. J., Dunne, J. P., Hiscock, M. R., Maritorena, S., ... Siegel, D. A. (2016). Annual cycles of phytoplankton biomass in the subarctic atlantic and pacific ocean. *Global Biogeochemical Cycles*, *30*(2), 175–190.

Wise, A., Calafat, F., Hughes, C., Jevrejeva, S., Katsman, C., Oelsmann, J., ... Richter, K. (2024). Using shelf-edge transport composition and sensitivity experiments to understand processes driving sea level on the Northwest European shelf. *Journal of Geophysical Research: Oceans*, *129*(5), e2023JC020587.

Xing, X., Morel, A., Claustre, H., Antoine, D., d'Ortenzio, F., Poteau, A., & Mignot, A. (2011). Combined processing and mutual interpretation of radiometry and fluorimetry from autonomous profiling Bio-Argo floats: Chlorophyll a retrieval. *Journal of Geophysical Research: Oceans*, *116*(C6).

Zhai, L., Gudmundsson, K., Miller, P., Peng, W., Gufinnsson, H., Debes, H., ... others (2012). Phytoplankton phenology and production around iceland and faroes. *Continental Shelf Research*, *37*, 15–25.

Zhang, X., Liu, L., Fei, J., Li, Z., Wei, Z., Zhang, Z., ... Xu, F. (2024). Advances in surface water and ocean topography for fine-scale eddy identification from altimeter sea surface height merging maps. *EGUsphere*, *2024*, 1–19.

Zhang, Z., Miao, M., Qiu, B., Tian, J., Jing, Z., Chen, G., ... Zhao, W. (2024). Submesoscale eddies detected by SWOT and moored observations in the Northwestern Pacific. *Geophysical Research Letters*, *51*(15), e2024GL110000.

Zhang, Z., Wang, W., & Qiu, B. (2014, July). Oceanic mass transport by mesoscale eddies. *Science*, *345*(6194), 322–324. doi: 10.1126/science.1252418

Zhao, J., Bower, A., Yang, J., Lin, X., & Penny Holliday, N. (2018b). Meridional heat transport variability induced by mesoscale processes in the subpolar North Atlantic. *Nature communications*, *9*(1), 1124.

Zhao, J., Bower, A., Yang, J., Lin, X., & Zhou, C. (2018a). Structure and formation of anticyclonic eddies in the Iceland Basin. *Journal of Geophysical Research: Oceans*, *123*(8), 5341–5359.